

Quantum correlations in electron microscopy

CHEN MECHEL,¹ YANIV KURMAN,¹ AVIV KARNIELI,² NICHOLAS RIVERA,³ ADY ARIE,² AND IDO KAMINER^{1,*} 

¹Solid State Institute, Technion, Israel Institute of Technology, 32000 Haifa, Israel

²School of Electrical Engineering, Tel Aviv University, Ramat Aviv 69978, Tel Aviv, Israel

³Department of Physics, Massachusetts Institute of Technology, 77 Massachusetts Avenue, Cambridge, Massachusetts 02139, USA

*Corresponding author: kaminer@technion.ac.il

Received 3 August 2020; revised 22 November 2020; accepted 23 November 2020 (Doc. ID 402693); published 11 January 2021

Electron microscopes provide a powerful platform for exploring physical phenomena with nanoscale resolution, based on the interaction of free electrons with the excitations of a sample such as phonons, excitons, bulk plasmons, and surface plasmons. The interaction usually results in the absorption or emission of such excitations, which can be detected directly through cathodoluminescence or indirectly through electron energy loss spectroscopy (EELS). However, as we show here, the underlying interaction of a free electron and an arbitrary optical excitation goes beyond what was predicted or measured so far, due to the interplay of entanglement and decoherence of the electron-excitation system. The entanglement of electrons and optical excitations can provide new analytical tools in electron microscopy. For example, it can enable measurements of optical coherence, plasmonic lifetimes, and electronic length scales in matter (such as the Bohr radius of an exciton). We show how these can be achieved using common configurations in electron diffraction and EELS, revealing significant changes in the electron's coherence, as well as in other quantum information theoretic measures such as purity. Specifically, we find that the purity after interaction with nanoparticles can only take discrete values, versus a continuum of values for interactions with surface plasmons. We quantify the post-interaction density matrix of the combined electron-excitation system by developing a framework based on macroscopic quantum electrodynamics. The framework enables a quantitative account of decoherence due to excitations in any general polarizable material (optical environment). This framework is thus applicable beyond electron microscopy. Particularly in electron microscopy, our work enriches analytical capabilities and informs the design of quantum information experiments with free electrons, allowing control over their quantum states and their decoherence by the optical environment. © 2021

Optical Society of America under the terms of the [OSA Open Access Publishing Agreement](https://doi.org/10.1364/OPTICA.402693)

<https://doi.org/10.1364/OPTICA.402693>

1. INTRODUCTION

Electron microscopy provides a powerful platform to study phenomena in condensed matter physics, optics, plasmonics, and many aspects of nanomaterials, all with the subnanometric precision of a free-electron probe. The most common techniques used for studying optical and material excitations are electron energy loss spectroscopy (EELS) [1–3] and cathodoluminescence [4,5]. More recent techniques also utilize the quantum wave nature of free electrons (e.g., by phase-front shaping [6–11] or by dressing electrons using a strong laser field [12–21]). Surprisingly, although these capabilities exploit the quantum wave properties of free electrons, other quantum features, such as the entanglement between the free electron and the optical excitations [22,23], have yet to be exploited.

One of the main footprints of entanglement of the electron with other quantum degrees of freedom in the environment is quantum decoherence [24–26]. Any observer measuring exclusively the electron usually loses knowledge of any coherence between the electron and the environment, since the environment was

left unobserved (“traced out”). A useful platform for observing the electron decoherence is the famous double-slit experiment [27,28] that continues to inspire new ideas in the field [29–31]. The first double-slit experiment that presented an interference pattern from a single electron was done in electron microscopes using electron holography [32–34]. Potapov *et al.* introduced a series of extensions of such double-slit experiments [35,36] in which free electrons interact inelastically with a (bulk) plasmonic excitation that serves as an effective “which-path” detector. Each electron's quantum coherence (transverse to its propagation) was measured using biprism-based holography. These experiments, and closely related theory [37], found that the spatial coherence of the inelastically scattered electron is highly correlated to the optical properties of the sample. In particular, the spatial coherence length is closely related to the propagation length of the bulk plasmon that is emitted [38–40].

From the discussion above, it should be clear that analyzing the quantum properties of free electrons has the potential to reveal

more information about the sample's excitations than conventional measures in electron microscopy. The remaining question is how to analyze the electron to unveil this additional information.

In this paper, we formulate a general theory of the entanglement and decoherence dynamics of electrons subject to interactions with an arbitrary optical environment. Using quantum information measures, we demonstrate how the formation of entanglement with the sample's optical excitations is correlated to spatial decoherence of the post-selected electron. We base our analytical calculations on macroscopic quantum electrodynamics (MQED) [41,42], which enables a fully quantum analysis of the interactions of electrons with electromagnetic fields in any optical environment, including absorbing and polarizable materials. This theory enables us to link the post-interaction electron density matrix with the quantum fluctuations of the electromagnetic field of the medium. Furthermore, we propose means of measuring and controlling the electron density matrix and specific properties such as decoherence by using standard electron microscopy techniques. We show the richness of coherence properties that the electron can inherit during its interaction with common nanostructures such as nanoparticles and thin metallic interfaces, comparing our results with experiments such as those of Ref. [35]. Our findings could help develop new analytical capabilities in electron microscopy. In particular, measuring the quantum coherence may enable probing the optical environment's quantum fluctuations through the electron's decoherence and help answer fundamental questions on the nature of light–matter interaction in the quantum regime.

Our approach provides the first quantum optical analysis of free-electron interaction with arbitrary electromagnetic environments. As opposed to bound-electron systems (such as atoms and quantum dots), examining arbitrary optical excitations using the continuous energy levels of the electron enables exploration of the wide range of phenomena in electron microscopy applications. In its classical limit, our formalism recovers the well-known EELS rates [2]. However, the formalism goes beyond the classical limit to unveil the underlying quantum correlations embedded in the free-electron probe. As a result, we strengthen the connection between the fields of electron microscopy and quantum information—a connection that has begun to emerge in recent years [22,23,43,44]. The motivation for our approach comes from previous works in electron microscopy and other free-electron systems that quantified electron decoherence [35–37,45,46]. The power of the MQED-based field quantization that we apply here is its generality: it enables one to link the properties of any optical environment directly to the electron image that is measured after the interaction.

To demonstrate intuitively the fundamental role of optical excitations in the quantum decoherence of free electrons, we illustrate in Fig. 1 a gedankenexperiment inspired by Refs. [35–37,47,48]. Consider a free electron impinging onto a thin metallic film and interacting with it [Figs. 1(a) and 1(b)]. During the interaction, the electron creates an optical excitation in the film, e.g., a surface plasmon polariton (SPP), and as a result, it loses one quantum of energy [49]. Then the electron passes through a double-slit apparatus (realized, for example, by an electron biprism [39,40,45,46,50]). A resulting interference pattern is obtained on a screen, from which the electron transverse coherence can be quantitatively measured via the fringe visibility.

In Figs. 1(a) and 1(b) we present the two possible extreme cases for the electron's transverse coherence. In Fig. 1(a), the excitation is very localized, for example, as a result of high propagation losses.

There, the post-interaction electron remains coherent only over a small area, so we expect no visible interference pattern on the screen. On the other hand, a large spatial coherence associated with a delocalized optical excitation manifests as a large spatial coherence of the post-interacted electron, and a visible interference pattern is observed [Fig. 1(b)]. From a quantum mechanical point of view, regardless of the spatial extent of the optical mode, the interacting electron is maximally entangled with the environment in both cases (see Supplement 1 Section S.4). However, the spatial width of the excitation determines the coherence length of the resulting electron. Thus, the usually unexplored properties of the optical environment, such as the spatial correlation functions of the electromagnetic field, can be extracted directly from measuring the electron's spatial coherence.

2. RESULTS

A. Theory for Analyzing Quantum Properties of a Post-Interaction Electron

In the spirit of the gedankenexperiment presented above, we consider the general case of an electron impinging on a sample of some structured optical medium, representing a general optical environment. The electron emits a quantum of an optical excitation hosted by this environment, leading to an entanglement of the electron and the optical excitation. Then the electron travels through an energy filter that post-selects electrons of a given energy before measuring its position or momentum [Fig. 1(c)].

The description of the interaction itself begins from the minimal coupling Hamiltonian of quantum electrodynamics (QED), acting as a perturbation on a free, relativistic electron, ignoring spin effects [51]. In this case, the Hamiltonian of the whole system is $H = H_e + H_{em} + H_{int}$, where the electron's Hamiltonian is $H_e = \mathbf{p}^2/2m\gamma$, the field's Hamiltonian (omitting the zero-point energy) is $H_{em} = \int d\mathbf{r} \int d\omega \hbar \omega \mathbf{f}^\dagger(\mathbf{r}, \omega) \cdot \mathbf{f}(\mathbf{r}, \omega)$, and $H_{int} = \frac{e}{m\gamma} \mathbf{A}(\mathbf{r}) \cdot \mathbf{p}$ describes the interaction term. In these equations, m denotes the electron mass, γ the Lorentz factor, \mathbf{p} the momentum operator of the paraxial electron, \mathbf{A} the quantized vector potential of the electromagnetic field, and $\mathbf{f}(\mathbf{r}, \omega)$ ($\mathbf{f}^\dagger(\mathbf{r}, \omega)$) the creation (annihilation) operator for a dipolar excitation in a medium. We write the electromagnetic vector potential $\mathbf{A}(\mathbf{r})$ in the second quantization in terms of these dipolar excitations as

$$\begin{aligned} \mathbf{A}(\mathbf{r}, \omega) = & \sqrt{\frac{\hbar}{\pi\epsilon_0}} \frac{1}{c^2} \int \omega d\omega \int d\mathbf{r}' \sqrt{\text{Im} \epsilon(\mathbf{r}', \omega)} \\ & \times \overset{=}{\mathbf{G}}(\mathbf{r}, \mathbf{r}', \omega) \hat{\mathbf{f}}(\mathbf{r}', \omega) + \text{h.c.}, \end{aligned} \quad (1)$$

where ϵ_0 is the vacuum permittivity, and c is the speed of light. The quantized field of Eq. (1) can be seen as an expression of the field resulting from a quantum dipole excitation at position \mathbf{r}' and frequency ω , oriented along a direction $j = x, y, z$. This excitation contributes to the vector potential in \mathbf{r} using the dyadic Green's function $\overset{=}{\mathbf{G}}(\mathbf{r}, \mathbf{r}', \omega)$ [41] as a propagator.

The joint state of the entire quantum system is obtained by combining the electron's state with the state of the electromagnetic field. Therefore, without loss of generality, the initial joint state of the system is a coherent electron wave function $|\psi_0\rangle_e$ and no field excitations $|0\rangle_{exc}$. The more general case of an incoherent electron

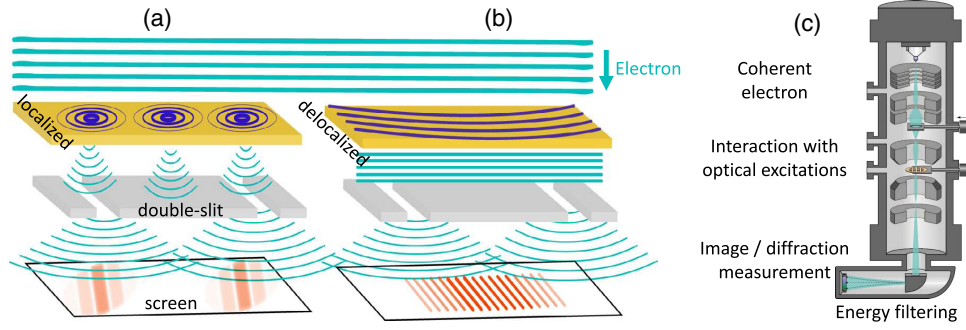


Fig. 1. Illustration of an electron interacting with an optical excitation as commonly realized in electron microscopes. Examples of electrons interacting with (a) localized and (b) delocalized optical excitations, which leave distinct footprints on the post-interaction electron. Such are manifested in the resulting interference patterns after the post-interaction electron propagates through two slits. The transverse coherence of the electron is measured on a screen at the bottom via the interference visibility, and it is strongly affected by the size of the excitations. In (a) and (b), the excitations are spatially localized/delocalized, respectively, compared to the distance between the slits, thereby preventing/preserving a visible interference pattern. (c) A transmission electron microscope, in which an electron can impinge on a thin metallic film to interact with optical excitations (plasmons). The microscope enables post-selected measurement of the electron’s position or momentum distribution by energy filtering, e.g., via the electron energy loss spectrometer (EELS) at the bottom of the figure.

is discussed in [Supplement 1](#) Section S.1.2. Assuming a weak interaction, the resulted entangled state is a coherent superposition, described as $|\psi_0\rangle_e|0\rangle_{\text{exc}} \xrightarrow{H_{\text{int}}} |\psi_0\rangle_e|0\rangle_{\text{exc}} + \sum_{\sigma} \sum_{\kappa} c_{\sigma\kappa} |\psi_{\sigma}\rangle_e |1_{\kappa}\rangle_{\text{exc}}$. In this summation, σ denotes the electron’s degrees of freedom (e.g., momentum, spin, energy, position) and κ the excitation’s degrees of freedom.

In usual EELS experiments, only the post-interaction electron is measured, whereas the sample (and its excitations) are left unmeasured [52]. From the perspective of quantum mechanics, this partial measurement corresponds to a partial trace over the sample degrees of freedom resulting in the electron’s reduced density matrix

$$\rho_c = \text{Tr}_{\text{exc}} \{ \rho_{\text{joint}} \} = \sum_{\sigma, \sigma'} \rho_c(\sigma, \sigma') |\psi_{\sigma}\rangle_e \langle \psi_{\sigma'}|_e \quad (2)$$

with the coefficients in the σ, σ' basis determined by $\rho_c(\sigma, \sigma') = \sum_{\kappa} c_{\sigma\kappa} c_{\sigma'\kappa}^*$. Therefore, the post-interaction electron is in a mixed state, comprised by an incoherent mixture of pure states, each corresponding to a different scattering outcome. This picture is equivalent to describing the electron as partially decohering as a result of the interaction.

To further develop Eq. (2), we use several approximations that are common in free-electron experiments and in electron microscopy. First, we assume the paraxial approximation for the motion of the electron beam, since typical angular spreads of such beams are on the order of a few milliradians or below. This approximation remains valid after the interaction as well, as given by the validity of the approximation that the electron recoils negligibly after interaction with an optical excitation (“no-recoil approximation”) [2]. Apart from the paraxial approximation, we also assume that the interaction occurs over a short distance relative to the post-interaction propagation distance to the detector, e.g., a few-micrometers evanescent field, compared to tens-of-centimeters distance to the detector. Such distances are also much longer than the typical (longitudinal) coherence length of each electron.

Under the assumptions above, the electron’s reduced density matrix after the interaction is given by (see [Supplement 1](#) Section S.1)

$$\rho_c(\mathbf{r}_T, \mathbf{r}'_T; \Delta E) = \frac{4\alpha}{\hbar c S} \int dz dz' e^{i \frac{\Delta E}{\hbar v_0} (z-z')} \times \text{Im} G_{zz} \left(\mathbf{r}_T, z; \mathbf{r}'_T, z'; \frac{\Delta E}{\hbar} \right). \quad (3)$$

Here z is coordinate along the electron propagation axis, ΔE is the electron energy loss, α is the fine-structure constant, v_0 is the initial electron speed, S is the electron beam area, and \hbar is the reduced Planck constant. The effect of the optical excitations is fully captured by the zz component of the imaginary part of the dyadic Green’s function. Importantly, the two transverse spatial arguments, \mathbf{r}_T and \mathbf{r}'_T , enable the determination of the transverse quantum coherence of the post-interaction electron via the off-diagonal elements of ρ_c . We note that the diagonal elements of the reduced density matrix, i.e., taking $\mathbf{r}_T = \mathbf{r}'_T$ in Eq. (3), retrieve the commonly used EELS probabilities for a point charge (found in [2]). In Eq. (3) we describe the density matrix in units of probability per unit energy per area, though it can be defined as probability per energy, which result in multiplying Eq. (3) by the electron transverse spot size. Equation (3) can be generalized to the case where the incoming electron is described by a general density matrix (see [Supplement 1](#) Section S.1.2 for full derivation). In this case, the electron final density matrix in the spatial coordinate basis is simply a product of Eq. (3) and its initial density matrix, which can be measured independently. This corresponds to a convolution of the momentum response of the sample with the electron’s initial density matrix in the momentum basis.

To demonstrate the implications of our new formalism and especially Eq. (3), we apply it to two types of archetypical optical excitations: propagating SPPs in thin metallic films and nanoparticles supporting localized optical modes. These two examples enable comparison of the effect of the excitation spectrum (e.g., whether it is continuous or discrete) on the post-interaction electron. These cases result in very different consequences in terms of the entanglement created during the interaction and, accordingly, the purity of the electron and its spatial coherence. In each case, we derive the resulting electron density matrix, discuss its properties, and show what the electron measurement can reveal about the optical excitation itself. We then present the connection between the two cases and highlight their differences and similarities.

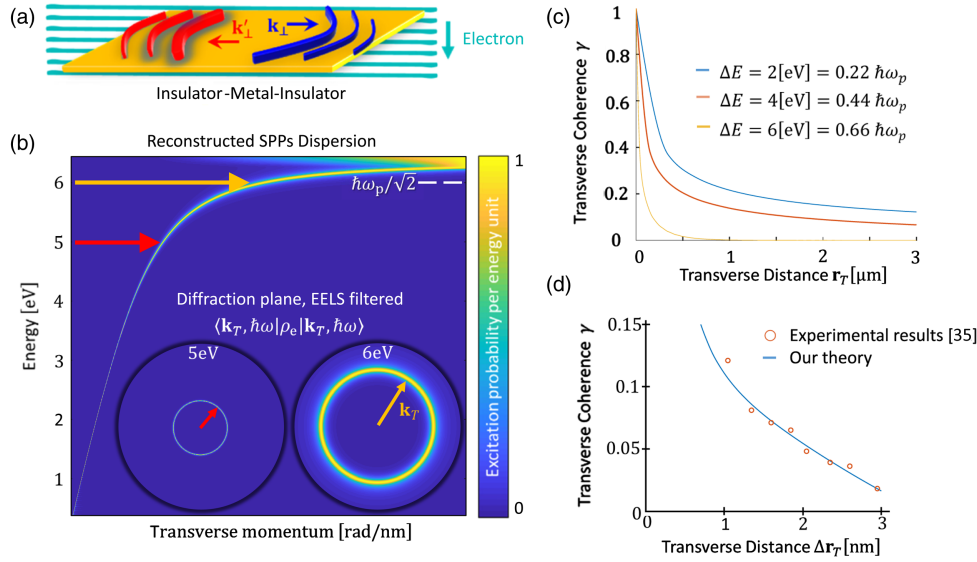


Fig. 2. Free-electron entanglement with surface plasmon polaritons (SPPs) to probe the SPP dispersion, lifetime, and coherence. (a) Schematic of the interaction. The electron moves through a thin insulator-metal-insulator interface hosting SPPs. The electron excites a plasmon and thus changes its energy and momentum in an amount equal to that of the plasmon, giving rise to electron-plasmon entanglement. Since each optical excitation is well described by its momentum, the density matrix is diagonal in that basis, and the complete density matrix of the electron at each energy can be obtained from a single energy-filtered diffraction image. (b) Reconstruction of the SPP dispersion and lifetime from EELS diffraction images for each energy loss $\hbar\omega$. Insets: two EELS diffraction images. The radius and width of each ring are used for the reconstruction of the dispersion curve. Each image shows the diagonal terms of the electron density matrix in the momentum basis for each energy, $\langle \mathbf{k}_T, \hbar\omega | \rho_e | \mathbf{k}_T, \hbar\omega \rangle$. The dispersion plot is constructed from the EELS diffraction image, calculated for each energy, as experimental data would be processed. (c) Electron transverse coherence as a function of the relative distance. The electron coherence grows with the propagation length of the plasmon, which decreases with energy. The calculations are based on Eq. (5), with simulated data from (b). (d) Same axes as in (c), but for bulk plasmons in aluminum (blue) and compared to the experimental results by [35] (red), giving a good fit. See Supplement 1 Section S.2.2 for fitting details and parameters.

B. First Case: Delocalized Excitations—Surface Plasmon Polaritons

The first case we present is the interaction of a free electron with SPPs as shown in Fig. 2(a). In this case, we show how the spatial coherence of the post-interaction electron is a convenient and reliable measurable quantity to analyze the optical excitation. In our example, the SPPs propagate along a thin metallic layer in a planar geometry (an insulator-metal-insulator, or IMI, structure). The system is translation invariant in the plane transverse to the electron's motion, so it is convenient to work in the transverse momentum basis for both the electron and the electromagnetic modes. Using this representation, we write the zz component of the electromagnetic Green's function of the sample [53]:

$$G_{zz}(\mathbf{r}_T, z; \mathbf{r}'_T, z'; \omega) = \frac{i}{8\pi^2} \frac{1}{(\omega/c)^2} \iint_{-\infty}^{\infty} r^P(\mathbf{k}_T, \omega) \times e^{i[\mathbf{k}_T \cdot (\mathbf{r}_T - \mathbf{r}'_T) + \frac{\omega}{c}(z + z')]} \mathbf{k}_T^2 d^2\mathbf{k}_T, \quad (4)$$

where $r^P(\mathbf{k}_T, \omega) = \frac{(\epsilon_r(\omega) - 1)i - \frac{\sigma(\omega)k_T}{\omega\epsilon_0}}{(\epsilon_r(\omega) + 1)i - \frac{\sigma(\omega)k_T}{\omega\epsilon_0}}$ is the momentum-dependent Fresnel reflection coefficient for p -polarized light, and $\epsilon_r(\omega)$ and $\sigma(\omega)$ are the frequency-dependent relative permittivity and conductivity of the metal (for the figures, we assume they follow the Drude model as discussed in Supplement 1 Section S.2.3).

Substituting Eq. (4) into Eq. (3), the resulting electron density matrix becomes

$$\rho_e(\mathbf{k}_T, \mathbf{k}'_T; \Delta E) = \frac{\delta(\mathbf{k}_T - \mathbf{k}'_T)}{S\hbar} \frac{16\pi^2\alpha c}{(\Delta E/\hbar)^2} \frac{\text{Im}\{r^P(\mathbf{k}_T, \Delta E/\hbar)\}}{\sqrt{k_T^2 - \frac{(\Delta E/\hbar)^2}{c^2}}} \times \frac{k_T^2}{k_T^2 - \frac{(\Delta E/\hbar)^2}{c^2} + \frac{(\Delta E/\hbar)^2}{v^2}}. \quad (5)$$

Due to the in-plane translational symmetry in the system, the density matrix is diagonal in the transverse momentum basis [manifested through $\delta(\mathbf{k}_T - \mathbf{k}'_T)$]. The diagonal elements depend on the post-selected energy loss ΔE and on the plasmonic spectral density of states in the specific energy and momenta [through $\text{Im}\{r^P(\mathbf{k}_T, \Delta E/\hbar)\}$]. Therefore, for each plasmonic energy, ρ_e is real-valued, positive, and depends on the transverse momentum transfer (\mathbf{k}_T) during the interaction. We note that, in this case, the azimuthal symmetry forces ρ_e to depend only on the magnitude of \mathbf{k}_T , and if the sample would be tilted, there would be an angular dependence.

In Fig. 2(b) we show the density matrix as a function of the magnitude of the momentum transfer k_T [and energy loss ΔE (vertical axis)], normalized for each plasmon energy. Due to energy and momentum conservation in the spontaneous emission process leading to EELS, the diagonal components of the density matrix are proportional to the energy and momentum-dependent excitation probability. Its peaks (in k_T - ω space) reveal the (complex) SPP dispersion relation. In experiments, the post-interaction electron goes through energy loss filtering, which leads to a ring-like diffraction image of the momentum-space electron state as illustrated in Fig. 2(b). The width of the ring is set by the momentum space width of the plasmon at that frequency, which is set

by the inverse propagation length. From this information, one can directly calculate the lifetime of the plasmon for each energy (limited by the electron zero-loss peak and by the resolution of the energy filter). Note that this approach is still limited by the energy resolution, which is affected by the initial electron energy spread (zero-loss peak) and the EELS resolution. This resolution determines the momentum resolution of the electron image and thus the resolution of both the dispersion curve and its width (see [54] for elaborated discussion). Note also that in terms of quantum measurement, we first post-select the electrons by energy and then measure their momentum distribution at the detector, which still obeys uncertainty relations.

Apart from the complex dispersion relation, the density matrix of Eq. (5) contains information regarding the loss of spatial coherence of the excitation, as the coherence length is connected to the propagation length. To quantify the SPP spatial coherence through the electron spatial coherence, we use a similar notation to that in optical coherence theory [55]. Due to the translation invariance of the system, the energy-filtered spatial coherence $\gamma(\mathbf{r}_T, \mathbf{r}'_T, \Delta E)$ depends solely on relative distance $\Delta \mathbf{r}_T$ and can be written as (see Supplement 1 Section S.2.1)

$$\gamma(\Delta \mathbf{r}_T, \Delta E) = \frac{\int \rho_e(\mathbf{k}_T) e^{i\mathbf{k}_T \cdot \Delta \mathbf{r}_T} d\mathbf{k}_T}{\int \rho_e(\mathbf{k}_T) d\mathbf{k}_T}, \quad (6)$$

where $\rho_e(\mathbf{k}_T)$ denotes the diagonal elements of ρ_e . Figure 2(c) presents γ in our structure for different conductivity values of the film and thus different propagation lengths L_p . Comparing it to Fig. 2(b), we find that larger losses correspond to shorter propagation lengths and higher spatial confinement of the optical modes. Therefore, the electron coherence area is greatly affected by the plasmonic losses in the material. This observation provides interesting possibilities for controlling the whole electron density matrix, for example, through controlling the sample temperature or charge carrier concentration via gate voltage. Additionally, this coherence function can be investigated for different propagation distances after the interaction; its propagation can be calculated using wave optics [55] as was done in electron microscopy [37,56]. It is important to note that although the electron beam area increases and refocuses in a microscope, the ratio between coherence and the beam width is known to be conserved [57], as the electron itself preserves its quantum coherence under any unitary operation.

Equation (6) indicates a way to measure $\gamma(\Delta \mathbf{r}_T, \Delta E)$ from the same energy-filtered diffraction images that are used for the reconstruction of the plasmonic dispersion. This measurement can be done by taking this diffraction image and calculating its two-dimensional Fourier transform, normalized by the total measured power. Note that the final electron coherence is also affected by the initial electron coherence; see Supplement 1 Sections S.1.2 and S.2.2.

We compare our theory to the experimental results from [35] for the case of bulk plasmons in Al samples and find a good match with our theory [see Fig. 2(d)]. Our findings explain the experimental results in terms of a general first-principles theory, in contrast to the previous structure-dependent approaches [37]. Since we only look at the electromagnetic response of the sample, an analogous calculation can be used to quantify the coherence size of any optical excitation, for example, the Bohr radius of an exciton [58].

Let us compare our approach (as performed, e.g., in [54,59]) with holography techniques that can also extract $\gamma(\Delta \mathbf{r}_T, \Delta E)$. We note that both are limited by the electron spatial coherence. However, there is a fundamental difference. Electron holography experiments in which one path undergoes inelastic scattering also suffer from temporal decoherence [35,36,50] (consequently, the duration of measurement alters the visibility since the different parts of the electron do not have the same energy). The scheme at the focus of our work does not involve the same temporal decoherence despite undergoing the same inelastic process. The reason is that the entire electron goes through an energy filter, and thus we only deal with a single electron energy (consequently, the duration of measurement does not alter the visibility) [38]. When holography is performed between two parts of an electron that have both undergone the same inelastic scattering process [60], there is similarly no temporal decoherence. We further note that the initial electron coherence affects the abovementioned methods in different ways. In holography, the fringe visibility decreases with reduced coherence, which could be compensated by increasing electron flux. In our approach, the initial electron coherence is convolved with the diffraction image. The preferred approach depends on a variety of factors, such as electron flux limitations (due to the sample or microscope), signal-to-noise ratio, and the momentum spread caused by the electron initial coherence compared to the plasmon mean momentum and spread.

C. Second Case: Localized Excitations in Nanoparticles

We now consider an electron interacting with a nanoparticle as illustrated in Fig. 3. In contrast to the previous case, the nanoparticles have a discrete number of electromagnetic modes that can be excited. As a result, we can analyze the system using concepts from quantum information in systems with discrete degrees of freedom, such as purity, which helps quantify the entanglement in the interaction. The nanoparticles can host optical excitations in the form of localized surface plasmons, whispering-gallery modes, or general cavity modes [61–63]. For simplicity, we consider the case in which the nanoparticles are far smaller than the electron beam area or the optical wavelength so we can regard them as point dipoles with a tensorial polarizability $\bar{\alpha}(\omega)$ (3 by 3 matrix). The polarizability tensor represents the nanoparticle's affinity to support a dipole moment in different directions and is affected by the nanoparticle geometry. Figure 3(a) depicts some examples of nanoparticles with different polarizability tensors and the corresponding electron energy-filtered images. The special cases presented in Fig. 3(a) show how one can analyze an arbitrary nanoparticle through the imaging of the energy-filtered electron.

The images of the electron are derived through the diagonal terms of the density matrix, obtained using Eq. (3) and the Green's function of a single dipolar particle. The optical excitations can be oriented along the direction of the electron velocity (z) or in the transverse plane ($x-y$), giving the electron three different electromagnetic potentials to interact with. As a result, the density matrix of the electron has longitudinal and transverse contributions. In particular, the density matrix in real space is given as

$$\rho_e(\mathbf{r}_T, \mathbf{r}'_T, \Delta E) = \frac{4\alpha}{c\hbar S} \left(\frac{\Delta E}{\hbar}\right)^2 \mu_0 \boldsymbol{\psi}(\mathbf{r}_T) \cdot \text{Im} \left\{ \bar{\alpha} \left(\frac{\Delta E}{\hbar}\right) \right\} \cdot \boldsymbol{\psi}^*(\mathbf{r}'_T), \quad (7)$$

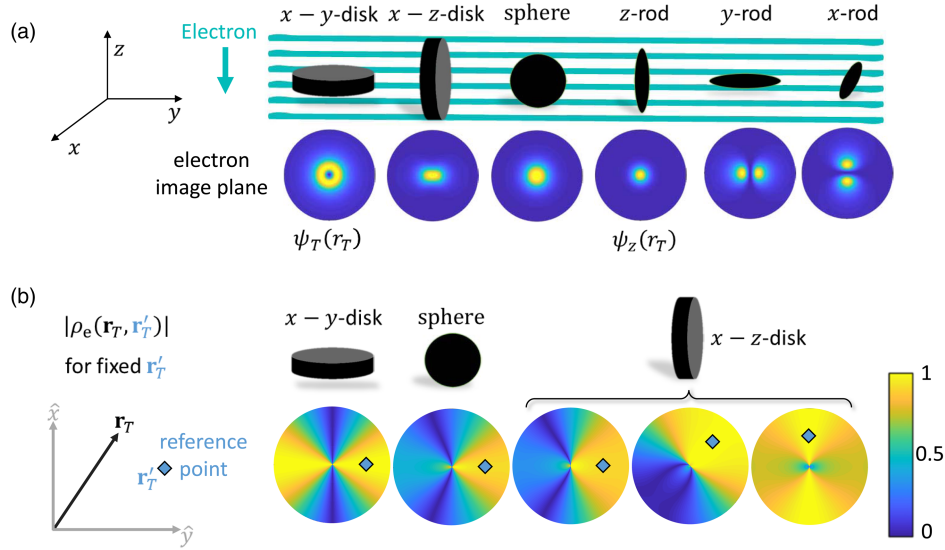


Fig. 3. Free-electron interaction with localized dipolar modes in nanoparticles. (a) Different shapes and orientations of nanoparticles, and each result in a different energy-filtered electron image for the interacting electron. The different dipole orientations induce very different electron images, which can be used to image the near field. All the images are shown with absolute value. (b) Electron coherence [normalized absolute value of $\rho_e(\mathbf{r}_T, \mathbf{r}'_T)$] for a fixed \mathbf{r}'_T (blue diamond). The three rightmost panels portray the coherence under the same $x-z$ -disk nanoparticle, with a different reference point \mathbf{r}'_T . The coherence has a strong angular dependence and a very slow radial decay. Thus, the electron is mostly spatially coherent within the transverse interaction area, yet different directions are incoherent with each other. As a reference, when exciting only single mode, the electron is perfectly coherent.

where μ_0 is the vacuum permeability, $\bar{\alpha}$ is the polarizability tensor, and $\boldsymbol{\psi}(\mathbf{r}_T) = \psi_T(r_T)\hat{\mathbf{r}}_T + \psi_z(r_T)\hat{\mathbf{z}}$. The function ψ_z describes the electron wave function after interacting with a purely longitudinal mode (a “ z -rod”) and ψ_T for an electron wave function after interacting with a purely transverse mode (an “ $x-y$ -disk”) as shown in Fig. 3(a). These functions can be calculated by considering the overlap between each optical mode and the electron’s initial wave function (see Supplement 1 Section S.3.1). From Eq. (7) we find that the electron density matrix is composed of an (incoherent) sum of the three different modes, weighted by the polarizability tensor of the nanoparticle. Thus, each term in the sum is associated with a different principal axis of the polarizability tensor $\bar{\alpha}(\omega)$.

The contribution of each electromagnetic mode on the electron is summed up incoherently in its density matrix. Thus, there is no interference between the different modes of excitation. Therefore, the spatial coherence of the electron depends on the relative excitation strength of different dipole orientations as seen in Fig. 3(b). As the electron excites more modes (e.g., a nanodisk or nanosphere, which support two and three modes, respectively), its spatial coherence is reduced as can be seen from the spatial coherence variation. Yet, since the number of available dipolar modes is discrete and limited to three dipole orientations, the electron remains mostly spatially coherent around the excitation point. Nevertheless, in all cases the coherence has a strong angular dependence that stems from the lack of coherence between different dipole orientations. However, when the electron interacts with a single electromagnetic mode per frequency, as in the nanorod case, it remains completely coherent at all angles.

Let us now explain these results in terms of the entanglement created during the interaction with the nanoparticle. We quantify the degree of entanglement using the purity measure

$$\text{purity} = \frac{\text{Tr}(\rho_e^2)}{\text{Tr}^2(\rho_e)}. \quad (8)$$

The purity measures the eigenvalue spread of a density matrix [64]; it equals unity for a pure electron state, and it gets a minimal value of $1/d$ for a maximally mixed state, where d is the dimension of the one-particle Fock space of the excitation. In the case of interactions with nanoparticles, the minimal purity value is $1/3$ ($d = 3$), while in the SPP case there is a continuum of modes (due to translational invariance), so d goes to infinity and the purity is zero (see Supplement 1 Section S.4). The electron’s purity is affected by its entanglement with the excitations: increasing their entanglement increases the quantum information contained in their joint state compared to each one’s state, decreasing the quantum information contained in the electron state alone, which increases the amount of nonzero eigenvalues in ρ_e and hence decreases its purity.

Figure 4 confirms that the electron’s purity is strongly related to the number of modes the nanoparticle can host. This corresponds to the number of nonzero eigenvalues of the polarizability tensor $\bar{\alpha}$ (see Supplement 1 Section S.3.2), which determines the number of eigenvalues of the electron density matrix. Consequently, the purity equals 1 if the electron interacts with a single electromagnetic mode, and it can take on rational values (e.g., $1/2$ and $1/3$) when each eigenmode is excited with equal probability. Therefore, the degree of entanglement between the electron and excitations can be adjusted by changing the relative excitation strength of the different optical modes. This can be done by rotating the nanoparticle [as in Fig. 4(b)], changing its aspect ratio (thus affecting the relative dipole moments along different directions), changing its permittivity, or simply by post-selecting different energies (which correspond to different modes altogether). This result leads to a fundamental conclusion: the degree of entanglement, and the respective electron decoherence, is primarily affected by the number of available optical excitations and their relative strength.

In general, direct observation of the results from Fig. 4 could be realized via interference experiments [34], quantum state

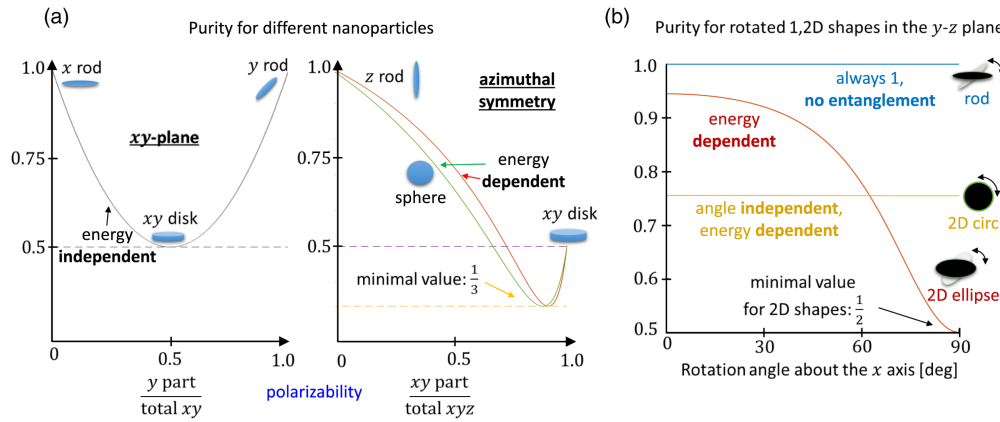


Fig. 4. Free-electron entanglement with excitations of nanoparticles of various forms/shapes: accessing discrete dimensionality of quantum information. (a) The electron purity for diagonal polarizability tensors representing various nanoparticle shapes. In the left half, the nanoparticles have their dipole moment in the $x-y$ plane. According to the number of eigenmodes, we find that for rods the purity is exactly 1, while for a circular disk the purity is exactly $1/2$. In the right panel, the shapes range from a z rod to an $x-y$ disk while keeping an $x-y$ (azimuthal) symmetry. The purity is found at its minimal value, exactly $1/3$, when the contributions from all the dipole orientations (x , y , z) are equal (three equal eigenvalues), corresponding to an oval-shaped nanoparticle. This figure demonstrates our control over the electron’s purity by shaping the nanoparticles’ classical dimensions, which directly controls the entanglement created in the interaction, in both discrete and continuous manners. The energy dependence stems from the fact that both longitudinal and transverse excitations are present, and each one has a different energy dependence. (b) Purity for one- and two-dimensional shapes in $y-z$, for rotations about the x axis. For 1D shapes (nanorods), there is only one excitable mode, so the entanglement vanishes and the purity is always 1. For the 2D shapes, the purity depends on the relative excitation strength of the z and the y dipoles. This depends both on rotation angle, and importantly on excitation energy, since the z -dipole excitation has a different energy dependence than the $x-y$ dipoles.

reconstruction [16], tomographic imaging [61], or cathodoluminescence coincidence [65]. However, using our theoretical analysis, one can connect classical-like observables (as cross-section images) to quantum phenomena (as entanglement), which enables inference of the entanglement in the interaction from standard electron intensity images. The entanglement, quantified by the electron’s purity, results from the fact that the electron experiences a different electromagnetic potential depending on the excited optical mode: x , y , or z dipoles. This dependence correlates the quantum wave function of the electron to the state of the nanoparticle, with different weights for each “option” (e.g., orientation), depending on the excitation probability of each option, and the tensorial polarizability of the nanoparticle. Using this knowledge of the electron density matrix, the electron purity can be calculated directly from a single measurement. In particular, this is done by fitting the polarizability tensor to the energy-filtered electron image (see Supplement 1 Section S.3.3 for further details).

Additionally, the electron-optical excitation entanglement can be tested in a direct manner, using experimental setups that implement coincidence measurements of EELS with light emission (cathodoluminescence) from plasmonic excitations, analogous to the coincidence experiment of [65] that correlated EELS and x -ray emission. These tests could be made to fully characterize the joint wave function of the electron and the plasmons or to perform experiments that test Bell’s inequality [66].

3. DISCUSSION AND SUMMARY

Let us now compare the two cases discussed above: the nanoparticle and SPP excitation. In the nanoparticle case, the number of excited modes is always discrete and is related to the geometrical properties of the nanostructure. The discrete number of modes implies that the electron’s reduced density matrix has a discrete set of eigenvalues, which results in a finite electron purity and slowly decaying

spatial coherence, in contrast with what might be expected from the gedankenexperiment of Fig. 1. The reason is that Fig. 1 relates to a SPP structure, where the electron’s spatial coherence corresponds to the SPP’s propagation length, and the eigenvalues of the electron density matrix enable finding the dispersion relation. However, the continuum of modes results in a vanishing purity (completely mixed electron), which is discussed more extensively in Supplement 1 Section S.4.

Coherently sculpting the electron wave function has been pursued in different experimental setups. Implementations include using elastic interactions in thin membranes [6–11] or by utilizing lasers [12–21,67], generally treating decoherence as a noise mechanism. Our work now paves the way towards sculpting the electron density matrix and its quantum decoherence using inelastic scattering. The control of the coupling strengths to each electromagnetic mode, as well as the mode’s confinement and lifetime, enables full control over the electron coherence and purity.

An example of such coherent sculpting can come with nanoparticles hosting multipolar modes [68,69] or multiple nanoparticles. Then the optical environment consists of more electromagnetic modes, which yields a higher dimensionality and thus a lower electron purity. Having several nanoparticles enables one to geometrically control the electron’s purity when changing the distance between the nanoparticles compared to the spatial extent of the electromagnetic modes. When the nanoparticles are optically separated, the electron’s quantum state is divided to independent Hilbert spaces. The interacting electron becomes entangled with this combined Hilbert space. When there is some spatial overlap between the different nanoparticle modes, the set of electromagnetic modes needs to be diagonalized in a way that usually removes degeneracies. Through the post-selected electron energy loss, one can control (post-select) an electron interaction with one of these modes. The above argument holds for electron interaction with any set of optical excitations. For example, a quantum dot exciton

strongly coupled to a plasmonic resonator (forming together two polaritonic modes) may also be probed by this technique, allowing for new probes of strong light–matter coupling.

Furthermore, our MQED-based formalism can be applied to more complex scenarios such as electron interaction with optical excitations that are pre-excited by an ultrashort laser pulse—a growing subfield of electron microscopy [12–23,67,70]. For such stimulated processes, it is possible to generalize the theories in [22,23] and in [2] using MQED [41]. There, due to the potentially high number of photon quanta in bosonic excitation, first-order perturbation theory is often not enough, necessitating higher-order calculations and even a nonperturbative analysis [71]. Additional interesting effects could be observed in cases of laser excitation of quantum emitters in the sample (e.g., in quantum dots, excitonic 2D materials, and nitrogen-vacancy centers), which can carry phase information. Then, the free-electron density matrix can capture information about the coherence of the initial excitation of the quantum emitter. The coherent phase information of the quantum emitter could potentially be extracted using specially shaped energy-modulated free electrons [70].

Additionally, our formalism could be extended to applications where time dynamics play a more central role in the interaction. Such applications may include optical environments with time-dependent properties (e.g., photonic time crystals [72–74]) and quantum emitters with time-dependent population dynamics (e.g., driven by ultrashort laser pulses), yielding different types of stimulated interactions. In case of a time-modulated permittivity, our formalism should be able to relate the temporal coherence in addition to its spatial coherence, which creates possibilities for entanglement in temporal degrees of freedom. The required mathematical extension is to calculate the electron density matrix's off-diagonal elements in the frequency space, in addition to the position space. This should be an interesting extension for our formalism, which we leave for future work.

To conclude, our work demonstrates how quantum information techniques can be exploited to expand the already rich analytical capabilities of electron microscopy. We presented a fully analytical and general description of free-electron interactions with quantized electromagnetic excitations, yielding the post-interaction electron density matrix. Using MQED, our analysis can be applied in any optical environment. Our theoretical predictions are in good agreement with existing experiments (e.g., based on holography), suggesting that the current phenomenological descriptions can be replaced by our first-principles theory. We showed how the optical fluctuations in the environment leave their footprints on the electron decoherence, and we analyzed the available quantum information in the electron using its spatial coherence and purity. Furthermore, we proposed means of measuring the coherence and lifetime of the optical excitations using simple electron measurements as well as means of controlling the electron coherence and purity (by shaping the electromagnetic environment). These capabilities can lead to many novel applications of existing electron microscopes.

Funding. European Union's Horizon 2020 research and innovation programme (851780-ERC-NanoEP); Israel Science Foundation (1415/17).

Acknowledgment. We thank Prof. Uri Sivan, Prof. Moti Segev and Prof. Jo Verbeeck for stimulating discussions. A.K. is

supported by the Adams Fellowship Program of the Israel Academy of Science and Humanities. N. R. is supported by the Department of Energy Fellowship DE-FG02-97ER25308 and by a Dean's Fellowship by the MIT School of Science.

Disclosures. The authors declare no conflicts of interest.

See Supplement 1 for supporting content.

REFERENCES AND NOTES

1. R. F. Egerton, "Electron energy-loss spectroscopy in the TEM," *Rep. Prog. Phys.* **72**, 016502 (2008).
2. F. G. De Abajo, "Optical excitations in electron microscopy," *Rev. Mod. Phys.* **82**, 209–275 (2010).
3. R. F. Egerton, *Electron Energy-Loss Spectroscopy in the Electron Microscope* (Springer, 2011).
4. L. Ozawa, *Cathodoluminescence: Theory and Applications* (Wiley-VCH, 1990).
5. A. Polman, M. Kociak, and F. J. G. de Abajo, "Electron-beam spectroscopy for nanophotonics," *Nat. Mater.* **18**, 1158–1171 (2019).
6. R. Danev and K. Nagayama, "Transmission electron microscopy with Zernike phase plate," *Ultramicroscopy* **88**, 243–252 (2001).
7. J. Verbeeck, H. Tian, and P. Schattschneider, "Production and application of electron vortex beams," *Nature* **467**, 301–304 (2010).
8. M. Uchida and A. Tonomura, "Generation of electron beams carrying orbital angular momentum," *Nature* **464**, 737–739 (2010).
9. B. J. McMorran, A. Agrawal, I. M. Anderson, A. A. Herzing, H. J. Lezec, J. J. McClelland, and J. Unguris, "Electron vortex beams with high quanta of orbital angular momentum," *Science* **331**, 192–195 (2011).
10. N. Voloch-Bloch, Y. Lereah, Y. Lilach, A. Gover, and A. Arie, "Generation of electron Airy beams," *Nature* **494**, 331–335 (2013).
11. R. Shiloh, Y. Lereah, Y. Lilach, and A. Arie, "Sculpturing the electron wave function using nanoscale phase masks," *Ultramicroscopy* **144**, 26–31 (2014).
12. B. Barwick, D. J. Flannigan, and A. H. Zewail, "Photon-induced near-field electron microscopy," *Nature* **462**, 902–906 (2009).
13. F. J. Garcia de Abajo, A. Asenjo-Garcia, and M. Kociak, "Multiphoton absorption and emission by interaction of swift electrons with evanescent light fields," *Nano Lett.* **10**, 1859–1863 (2010).
14. S. T. Park, M. Lin, and A. H. Zewail, "Photon-induced near-field electron microscopy (PINEM): theoretical and experimental," *New J. Phys.* **12**, 123028 (2010).
15. A. Feist, K. E. Echternkamp, J. Schauss, S. V. Yalunin, S. Schäfer, and C. Ropers, "Quantum coherent optical phase modulation in an ultrafast transmission electron microscope," *Nature* **521**, 200–203 (2015).
16. K. E. Priebe, C. Rathje, S. V. Yalunin, T. Hohage, A. Feist, S. Schäfer, and C. Ropers, "Attosecond electron pulse trains and quantum state reconstruction in ultrafast transmission electron microscopy," *Nat. Photonics* **11**, 793–797 (2017).
17. E. Pomarico, I. Madan, G. Berruto, G. M. Vanacore, K. Wang, I. Kaminer, and F. Carbone, "meV resolution in laser-assisted energy-filtered transmission electron microscopy," *ACS Photon.* **5**, 759–764 (2017).
18. Y. Morimoto and P. Baum, "Diffraction and microscopy with attosecond electron pulse trains," *Nat. Phys.* **14**, 252–256 (2018).
19. G. M. Vanacore, G. Berruto, I. Madan, E. Pomarico, P. Biagioni, R. J. Lamb, D. McGrouther, O. Reinhardt, I. Kaminer, B. Barwick, H. Larocque, V. Grillo, E. Karimi, F. J. Garcia de Abajo, and F. Carbone, "Ultrafast generation and control of an electron vortex beam via chiral plasmonic near fields," *Nat. Mater.* **18**, 573–579 (2019).
20. K. Wang, R. Dahan, M. Shentcic, Y. Kauffmann, A. Ben Hayun, O. Reinhardt, S. Tesses, and I. Kaminer, "Coherent interaction between free electrons and a photonic cavity," *Nature* **582**, 50–54 (2020).
21. O. Kfir, H. Lourenco-Martins, G. Storeck, M. Sivis, T. R. Harvey, T. J. Kippenberg, A. Feist, and C. Ropers, "Controlling free electrons with optical whispering-gallery modes," *Nature* **582**, 46–49 (2020).
22. V. Di Giulio, M. Kociak, and F. J. G. de Abajo, "Probing quantum optical excitations with fast electrons," *Optica* **6**, 1524–1534 (2019).
23. O. Kfir, "Entanglements of electrons and cavity photons in the strong-coupling regime," *Phys. Rev. Lett.* **123**, 103602 (2019).

24. A. Stern, Y. Aharonov, and Y. Imry, "Phase uncertainty and loss of interference: a general picture," *Phys. Rev. A* **41**, 3436–3448 (1990).
25. Y. Imry, *Introduction to Mesoscopic Physics (No. 2)* (Oxford University Press on Demand, 2002).
26. K. Hornberger, S. Gerlich, P. Haslinger, S. Nimmrichter, and M. Arndt, "Quantum interference of clusters and molecules," *Rev. Mod. Phys.* **84**, 157–173 (2012).
27. R. P. Feynman, *The Feynman Lectures on Physics* (Narosa, 1965), Vol. **3**.
28. E. Buks, R. Schuster, M. Heiblum, D. Mahalu, and V. Umansky, "Dephasing in electron interference by a 'which-path' detector," *Nature* **391**, 871–874 (1998).
29. F. S. Yasin, K. Harada, D. Shindo, H. Shinada, B. J. McMorran, and T. Tanigaki, "A tunable path-separated electron interferometer with an amplitude-dividing grating beamsplitter," *Appl. Phys. Lett.* **113**, 233102 (2018).
30. K. Harada, T. Akashi, K. Niitsu, K. Shimada, Y. A. Ono, D. Shindo, H. Shinada, and S. Mori, "Interference experiment with asymmetric double slit by using 1.2-MV field emission transmission electron microscope," *Sci. Rep.* **8**, 1–10 (2018).
31. A. H. Tavabi, C. B. Boothroyd, E. Yücelen, S. Frabboni, G. C. Gazzadi, R. E. Dunin-Borkowski, and G. Pozzi, "The Young-Feynman controlled double-slit electron interference experiment," *Sci. Rep.* **9**, 1–8 (2019).
32. P. G. Merli, G. Missiroli, and G. Pozzi, "On the statistical aspect of electron interference phenomena," *Am. J. Phys.* **44**, 306–307 (1976).
33. A. Tonomura, "Electron holography," in *Electron Holography* (Springer, 1999), pp. 29–49.
34. A. Orchowski, W. D. Rau, and H. Lichte, "Electron holography surmounts resolution limit of electron microscopy," *Phys. Rev. Lett.* **74**, 399–402 (1995).
35. P. L. Potapov, H. Lichte, J. Verbeeck, and D. Van Dyck, "Experiments on inelastic electron holography," *Ultramicroscopy* **106**, 1012–1018 (2006).
36. P. L. Potapov, J. Verbeeck, P. Schattschneider, H. Lichte, and D. Van Dyck, "Inelastic electron holography as a variant of the Feynman thought experiment," *Ultramicroscopy* **107**, 559–567 (2007).
37. J. Verbeeck, D. Van Dyck, H. Lichte, P. Potapov, and P. Schattschneider, "Plasmon holographic experiments: theoretical framework," *Ultramicroscopy* **102**, 239–255 (2005).
38. Note that there is a difference between the spatial decoherence that we study here and the temporal decoherence that arises in interference of electron parts with different energies, e.g., where part of the electron undergoes inelastic scattering [39,40]. The spatial decoherence arises for electrons of a single energy value, e.g., for energy-filtered imaging or diffraction. Consequently, such decoherence measurements are not altered by the duration of measurement.
39. J. Verbeeck, G. Bertonni, and H. Lichte, "A holographic biprism as a perfect energy filter?" *Ultramicroscopy* **111**, 887–893 (2011).
40. D. Van Dyck, H. Lichte, and J. C. H. Spence, "Inelastic scattering and holography," *Ultramicroscopy* **81**, 187–194 (2000).
41. S. Scheel and S. Y. Buhmann, "Macroscopic quantum electrodynamics-concepts and applications," *Acta Phys. Slovaca* **58**, 675–809 (2008).
42. N. Rivera, I. Kaminer, B. Zhen, J. D. Joannopoulos, and M. Soljačić, "Shrinking light to allow forbidden transitions on the atomic scale," *Science* **353**, 263–269 (2016).
43. R. Remez, A. Karnieli, S. Trajtenberg-Mills, N. Shapira, I. Kaminer, Y. Lereah, and A. Arie, "Observing the quantum wave nature of free electrons through spontaneous emission," *Phys. Rev. Lett.* **123**, 060401 (2019).
44. O. Reinhardt, C. Mechel, M. Lynch, and I. Kaminer, "Free-electron qubits," *Analen der Physik, Early View* (2020).
45. P. Sonntag and F. Hasselbach, "Measurement of decoherence of electron waves and visualization of the quantum-classical transition," *Phys. Rev. Lett.* **98**, 200402 (2007).
46. N. Kerker, R. Röpke, L. M. Steinert, A. Pooch, and A. Stibor, "Quantum decoherence by Coulomb interaction," *New J. Phys.* **22**, 063039 (2020).
47. F. Röder and H. Lichte, "Inelastic electron holography—first results with surface plasmons," *Eur. Phys. J. Appl. Phys.* **54**, 33504 (2011).
48. P. Schattschneider and H. Lichte, "Correlation and the density-matrix approach to inelastic electron holography in solid state plasmas," *Phys. Rev. B* **71**, 045130 (2005).
49. One can apply an energy filter to post-select electrons that lost exactly one quanta of plasmon energy.
50. H. Lichte and M. Lehmann, "Electron holography—basics and applications," *Rep. Prog. Phys.* **71**, 016102 (2007).
51. I. Kaminer, M. Mutzafi, A. Levy, G. Harari, H. H. Sheinfux, S. Skirlo, J. Nemirovsky, J. D. Joannopoulos, M. Segev, and M. Soljacic, "Quantum Čerenkov radiation: spectral cutoffs and the role of spin and orbital angular momentum," *Phys. Rev. X* **6**, 011006 (2016).
52. From the point of view of quantum information, this is the opposite case to cathodoluminescence in scanning electron microscopes, in which the emitted light is measured while the electron is not.
53. L. Novotny and B. Hecht, *Principles of Nano-Optics* (Cambridge University, 2012).
54. G. Bertonni, J. Verbeeck, and F. Brosens, "Fitting the momentum dependent loss function in EELS," *Microsc. Res. Tech.* **74**, 212–218 (2011).
55. L. Mandel and E. Wolf, *Optical Coherence and Quantum Optics* (Cambridge University, 1995).
56. J. Verbeeck, G. Bertonni, and P. Schattschneider, "The Fresnel effect of a defocused biprism on the fringes in inelastic holography," *Ultramicroscopy* **108**, 263–269 (2008).
57. G. Pozzi, "Theoretical considerations on the spatial coherence in field emission electron microscope," *Optik* **77**, 69–73 (1987).
58. A. Polimeni, G. B. H. von Högersthal, F. Masia, A. Frova, M. Capizzi, S. Sanna, and W. Stolz, "Tunable variation of the electron effective mass and exciton radius in hydrogenated GaAs 1-x N x," *Phys. Rev. B* **69**, 041201 (2004).
59. J. Verbeeck, D. Van Dyck, and G. Van Tendeloo, "Energy-filtered transmission electron microscopy: an overview," *Spectrochim. Acta, Part B* **59**, 1529–1534 (2004).
60. F. Röder and A. Lubk, "Transfer and reconstruction of the density matrix in off-axis electron holography," *Ultramicroscopy* **146**, 103–116 (2014).
61. A. Hörl, G. Haberfehlner, A. Trügler, F. P. Schmidt, U. Hohenester, and G. Kothleitner, "Tomographic imaging of the photonic environment of plasmonic nanoparticles," *Nat. Commun.* **8**, 1–7 (2017).
62. M. R. Foreman, D. Keng, J. R. Lopez, and S. Arnold, "Whispering gallery mode single nanoparticle detection and sizing: the validity of the dipole approximation," *Opt. Lett.* **42**, 963–966 (2017).
63. U. Hohenester, H. Ditlbacher, and J. R. Krenn, "Electron-energy-loss spectra of plasmonic nanoparticles," *Phys. Rev. Lett.* **103**, 106801 (2009).
64. M. A. Nielsen and I. Chuang, *Quantum Computation and Quantum Information* (2002).
65. D. Jannis, K. Müller-Caspary, A. Béch e, A. Oelsner, and J. Verbeeck, "Spectroscopic coincidence experiments in transmission electron microscopy," *Appl. Phys. Lett.* **114**, 143101 (2019).
66. J. S. Bell, "On the Einstein Podolsky Rosen paradox," *Phys. Phys. Fiz.* **1**, 195–290 (1964).
67. Y. Pan, B. Zhang, and A. Gover, "Anomalous photon-induced near-field electron microscopy," *Phys. Rev. Lett.* **122**, 183204 (2019).
68. C. T. Tai, "On the eigenfunction expansion of dyadic Green's functions," *Proc. IEEE* **61**, 480–481 (1973).
69. C. T. Tai, *Dyadic Green Functions in Electromagnetic Theory* (Institute of Electrical & Electronics Engineers (IEEE), 1994).
70. O. Reinhardt and I. Kaminer, "Theory of shaping electron wavepackets with light," *ACS Photon.* **7**, 2859–2870 (2020).
71. N. Rivera and I. Kaminer, "Light-matter interactions with photonic quasi-particles," *Nat. Rev. Phys.* **2**, 538–561 (2020).
72. F. Biancalana, A. Amann, A. V. Uskov, and E. P. O' Reilly, "Dynamics of light propagation in spatiotemporal dielectric structures," *Phys. Rev. E* **75**, 46607 (2007).
73. J. R. Zurita-Sánchez, P. Halevi, and J. C. Cervantes-González, "Reflection and transmission of a wave incident on a slab with a time-periodic dielectric function $\epsilon(t)$," *Phys. Rev. A* **79**, 53821 (2009).
74. E. Lustig, Y. Sharabi, and M. Segev, "Topological aspects of photonic time crystals," *Optica* **5**, 1390–1395 (2018).